

# Capacitive-Type Two-Axis Accelerometer with Liquid-Type Proof Mass

Dong-Joon Won, Myoung Huh, Sangmin Lee, Usung Park, Dongwoo Yoo, and Joonwon Kim\*

Utilizing the advantages of a liquid metal (LM) (i.e., mercury) and its electro-mechanical properties (i.e., high density, high surface tension, and high electrical conductivity), a novel capacitive-type two-axis accelerometer is proposed. The device employs a liquid-type proof mass (i.e., liquid metal droplet) and is located in a cone-shaped guiding channel. The Laplace pressure induced by the guiding channel and the LM droplet in the device acts as a spring due to the high surface tension of LM. To accurately set the spring constant of the device, a 2D mathematical model is established. Based on this mathematical model, the influence of the channel shape on device sensitivity is analyzed. Despite measuring the two-axis accelerations using a single proof mass, the accelerometer yields a cross-axis sensitivity of less than 1% for the *x*- and *y*-axes. The accelerometer demonstrates an output similar to that of a reference accelerometer for a randomly applied acceleration. Owing to the nature of the liquid-type proof mass, even if it is destroyed, its functionality is recovered by simply shaking the accelerometer. Finally, a 1.4% change in the accelerometer output is observed in the 15 000-cycle test, and the device is applied to a maze escape game for verification.

of mass.<sup>[2]</sup> To measure the position, various accelerometers have been developed, such as capacitive,<sup>[3–14]</sup> piezoresistive,<sup>[15,16]</sup> resonant,<sup>[17,18]</sup> and optical<sup>[19,20]</sup> accelerometers. However, accelerometers with such microscale solid spring-like silicon structures can suffer from mechanical fatigue.<sup>[21,22,23,24]</sup> Various studies have been conducted to solve these problems. Moreover, efforts have been made to increase the lifetime through design<sup>[25,26]</sup> and packaging<sup>[24,27]</sup> methods. However, these approaches complicate the fabrication process. To avoid and minimize fatigue, accelerometers that do not comprise solid moving parts have been developed.<sup>[28–30]</sup>

One of the accelerometers without solid moving parts is by utilizing the advantages of a liquid metal (LM) (i.e., mercury) and its electro-mechanical properties (i.e., high density, high surface tension, and electrical conductivity). The main advantage of the LM accelerometer is that the

proof mass (i.e., high density) and spring-like structure (i.e., high surface tension) are combined together in the form of a droplet to avoid mechanical fatigue and simplify the fabrication process. If the solid moving part of a conventional accelerometer is replaced with a liquid component, a relatively simple, fatigue free mechanical accelerometer can be realized.

There are two representative accelerometer approaches that employ LMs. In the first approach, disconnected electrodes are connected when a conductive LM droplet passes over them.<sup>[31]</sup> However, the disadvantage of this structure is that acceleration can only be measured in a single direction, owing to the diamond-shaped channel, and the discrete position is measured. In the second approach, the position of the LM droplet is measured using a property wherein current flows to the root with low resistance. The accelerations of the two axes are continuously measured using a cone-shaped channel and four electrodes patterned in the *x*- and *y*-directions, respectively.<sup>[32]</sup> However, the relationship between the channel shape and Laplace pressure is yet to be identified. Both devices employ glass substrates as the electrodes, which has a relatively high sliding angle of  $\approx 15^\circ$ .<sup>[33]</sup> Therefore, they exhibit poor mobility of the LM droplet. A surface modification can lower the sliding angle; however, this is difficult owing to the presence of electrodes on the surface. If surface modification is applied, the electrodes can be damaged.

## 1. Introduction

Acceleration measurements are essential in several systems ranging from consumer electronics to healthcare systems.<sup>[1,2]</sup> Generally, the major components of a micro-fabricated accelerometer are a solid proof mass and the spring-like structures supporting the proof mass. When acceleration is applied to accelerometers, the mass moves deforming the spring, and the input acceleration is calculated by measuring the position

D.-J. Won, M. Huh, D. Yoo, Prof. J. Kim  
Department of Mechanical Engineering  
Pohang University of Science and Technology (POSTECH)  
Pohang, Gyeongbuk 37673, South Korea  
E-mail: joonwon@postech.ac.kr

Prof. S. Lee  
Division of Mechanical, Automotive and Robot Component Engineering  
Dong-Eui University  
Busan 47340, South Korea

Dr. U. Park  
The 3rd R&D Institute, Agency for Defense Development  
Daejeon 34186, South Korea

 The ORCID identification number(s) for the author(s) of this article can be found under <https://doi.org/10.1002/aelm.201901265>.

DOI: 10.1002/aelm.201901265

**Table 1.** Performance comparison of different types of accelerometers.

Type of proof mass	Type	Proof mass size [mm <sup>3</sup> ]	Sensitivity x, y, and z [fF g <sup>-1</sup> ]	Cross-axis sensitivity x, y, and z [%]	Range [±g]	Nonlinearity x, y, and z [%]	Noise [μg/rt-Hz]	Ref.
Solid	Single-axis (capacitive)	4.5 × 4.75 × 0.05	110	–	≈7	2 [±7 g]	≈120 μV/rt-Hz	[8]
		–	11.2	–	5	0.11	11.5	[9]
	Dual-axis (capacitive)	0.6 × 0.6 × 0.012	≈0.58	–	7.5 (x) 2.5 (y)	–	0.29, 1.2	[10]
		1.8 × 1.8 × 0.03	≈27	–	5 (x, y)	1.01'	–	[11]
	Tri-axis (capacitive)	1.78 × 1.38 × 0.007	0.53, 0.28, 0.2 [mV g <sup>-1</sup> ]	<7.46, <8.05, <8.33	0.8–6	2.64, 3.15, 3.36	120 000, 271 000, 357 000	[12]
		0.4 × 0.4 × 0.0088	14.7, 15.4, 14.6 [mV g <sup>-1</sup> ]	6.6, 5.4, 5.3	0–1	3.2, 1.4, 2.8	2100, 2000, 2100	[13]
		–	0.24, 0.24, 0.82	1.58 (calculated)	11 (x, y), 5.5 (z)	–	730, 730, 760	[14]
Liquid	Single-axis (connecting)	1.6 μL	–	–	≈40	–	–	[31]
	Dual-axis (resistive)	10 μL	≈6 (x), ≈4 (y) [kΩ g <sup>-1</sup> ]	2.7 (x), 1.2 (y)	–	11.7 (x) <sup>[32]</sup> 7.45 (y) <sup>[32]</sup> (calculated)	–	[32]
	Dual-axis (capacitive)	8 μL	≈350 (x, y) (calculated)	0.2 (x), 0.8 (y)	<≈5	5.9 [±1 g]	3272	This work

In this paper, a capacitive-type two-axis accelerometer using an LM droplet is proposed. To control the sensitivity of the device, it is necessary to accurately determine the spring constant, which depends on the shape of the guiding channel and volume of the LM droplet. Thus, Laplace pressure applied to the position of LM droplet in the guiding channel is accurately calculated using a 2D mathematical model. The effect of channel shape on spring constant of the device is then analyzed using a mathematical model. The position of LM droplet is measured by sensing an overlapped area between the liquid metal droplet and electrodes. To improve the response of the device, a method for measuring the capacitance using a floating electrode concept<sup>[34]</sup> is applied which also increases the mobility of LM. Because the dielectric layer enables a surface modification without damage to the electrode, the contact surfaces of the liquid metal have low resistance to move the droplet. Additionally, common sensor characteristics (i.e., the cross-axis sensitivity, response time, shake-recoverable characteristic, temperature behavior, and repeatability) are measured and analyzed. The device was verified in a consumer electronic application and applied to a maze escape game, wherein it was demonstrated that it worked successfully. **Table 1** compares the characteristics of general accelerometers and the developed sensor.

## 2. Sensing Principle and Device Configuration

### 2.1. Sensing Principle

To measure the position of the LM droplet in the channel, a floating electrode concept is used (**Figure 1a**).<sup>[34]</sup> When acceleration is applied, the position of the liquid metal is changed due to

the inertial force. Subsequently, the position of the LM droplet is estimated by sensing the change in the overlapped area ( $\Delta A$ ) between the LM droplet and the electrodes (**Figure 1b**). In the device, Laplace pressure caused by the movement of LM droplet in the cone shaped guiding channel acts as a force moving the droplet to the center, which in turn reacts as a restoring force of a spring in a typical accelerometer (**Figure 1c**). The capacitance changes with variation in the overlapped area between LM droplet and bottom electrode pairs. As the overlapped area between LM droplet and electrode pair widens, Cap. 1 and Cap. 2 increase along with an overall capacitance (**Figure 1d**). Herein, the LM droplet and bottom electrode pairs are separated using PSA tape, which acts as a dielectric layer. The changes in capacitance (i.e., Cap. 1 and Cap. 2) according to a change in the overlapped area<sup>[34]</sup> between the LM droplet and bottom electrode are shown in Equation (1).

$$\Delta C = \epsilon_0 \epsilon_r \Delta A/d \quad (1)$$

where  $\Delta C$ ,  $\epsilon_0$ ,  $\epsilon_r$ ,  $\Delta A$ , and  $d$  represent the capacitance change, vacuum permittivity, dielectric constant, change in overlapping area between the LM droplet and bottom electrode, and thickness of the dielectric layer, respectively.

Unlike previous studies, this study utilizes a capacitive-type mechanism, to perform sandblasting on all surfaces that are in contact with liquid metal droplets. **Figure 1e** shows the comparison between signal output of the device with and without sandblasting, under the same acceleration (**Movie S1**, Supporting Information). It can be seen that the signal of the device without sandblasting has a time delay of ≈25 ms as compared to the signal of the device with sandblasting. Additionally, it can also be noted from the signal sizes, that the device with sandblasting has a higher sensitivity than that without.

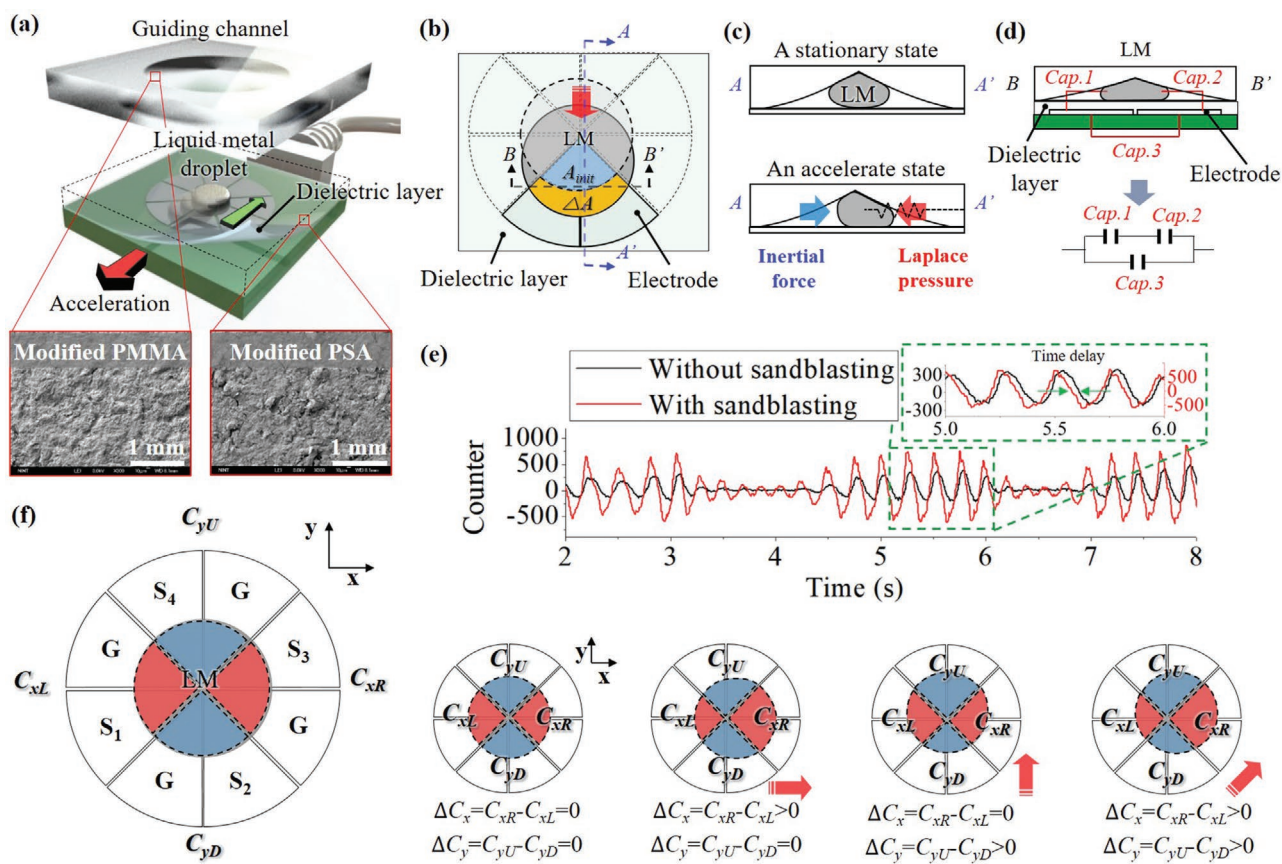


**Figure 1.** a) The schematic of sensing part (floating electrode concept). Modified surfaces on the guiding channel and dielectric layer (double side modification). b) Change in overlapped area ( $\Delta A$ ) between the liquid metal droplet and electrode pairs according to the acceleration. c) Cross-sectional view of AA' Laplace pressure and inertial force induced in the guiding channel under an accelerated state. d) Cross-sectional view of BB' and schematic relationship of each capacitance value (i.e., Cap. 1, Cap. 2, and Cap. 3). e) Comparison signal output of the device between the with and without sandblasting under the same acceleration. f) Expected capacitance variations for various cases of acceleration.

Because the device has eight cells of electrodes (Figure 1f), these cells can be divided into four cell pairs each in the  $x$ - and  $y$ -axes directions (i.e., for the  $x$ -axis,  $C_{xL}$  ( $S_1$  and G pairs) and  $C_{xR}$  ( $S_3$  and G pairs), and for the  $y$ -axis,  $C_{yU}$  ( $S_4$  and G pairs) and  $C_{yD}$  ( $S_2$  and G pairs)). The applied acceleration is measured by calculating the difference in capacitance ( $\Delta C$ ) between the opposing cell pairs along each axis. Dividing the electrode further would increase the accuracy of the direction; however, this would reduce  $\Delta C$  due to a decrease of  $\Delta A$  when LM travels the same distance. Furthermore, as a smaller  $\Delta C$  would incur a greater effect of noise in the measurement system ( $\approx \pm 20$  counter), larger sensing electrodes are required. Therefore, to achieve this, the design was created with a minimum number of electrodes (i.e., eight cells) to distinguish the direction of the applied biaxial acceleration.

The expected variations in capacitance for various accelerations are presented in Figure 1f. The guiding channel restricts the radial movement of the LM droplet due to the Laplace pressure. When acceleration is not applied, the droplet is held at the center of the electrodes, and the overlapped areas between the droplet and all the cell pairs are the same in all directions; the differences in capacitance of each cell pair are the same (i.e.,  $\Delta C_x = C_{xR} - C_{xL} = 0$ ,  $\Delta C_y = C_{yU} - C_{yD} = 0$ ). However, when

acceleration is applied, the droplet moves through the inertia force. As the droplet moves from the center of the cells, the overlapped areas between the droplet and cell pairs change, which results in differences in the capacitance of these pairs (e.g.,  $\Delta C_x = C_{xR} - C_{xL} \neq 0$ ,  $\Delta C_y = C_{yU} - C_{yD} \neq 0$ ).

## 2.2. Device Configuration

The accelerometer prototype has a sensor part with an LM droplet and a package part, as shown in Figure 2a. The sensor part consists of a floating electrode (LM droplet), a guiding channel, a dielectric layer, and sensing electrodes that are radially patterned on a printed circuit board (PCB). To accurately align the sensing PCB and guiding channel in the assembly process, upper and lower aligners are designed. To improve the sensitivity by reducing the electrical noise from the environment, copper sheet tape used for shielding is attached to both the aligner parts and connected to the ground. The thickness of the aligner is designed such that a distance of 3 mm is maintained between the sensing electrodes and the shielding pad. Finally, aluminum cases are created to prevent damage to the inner parts. Moreover, the sensing PCB and guiding channel are

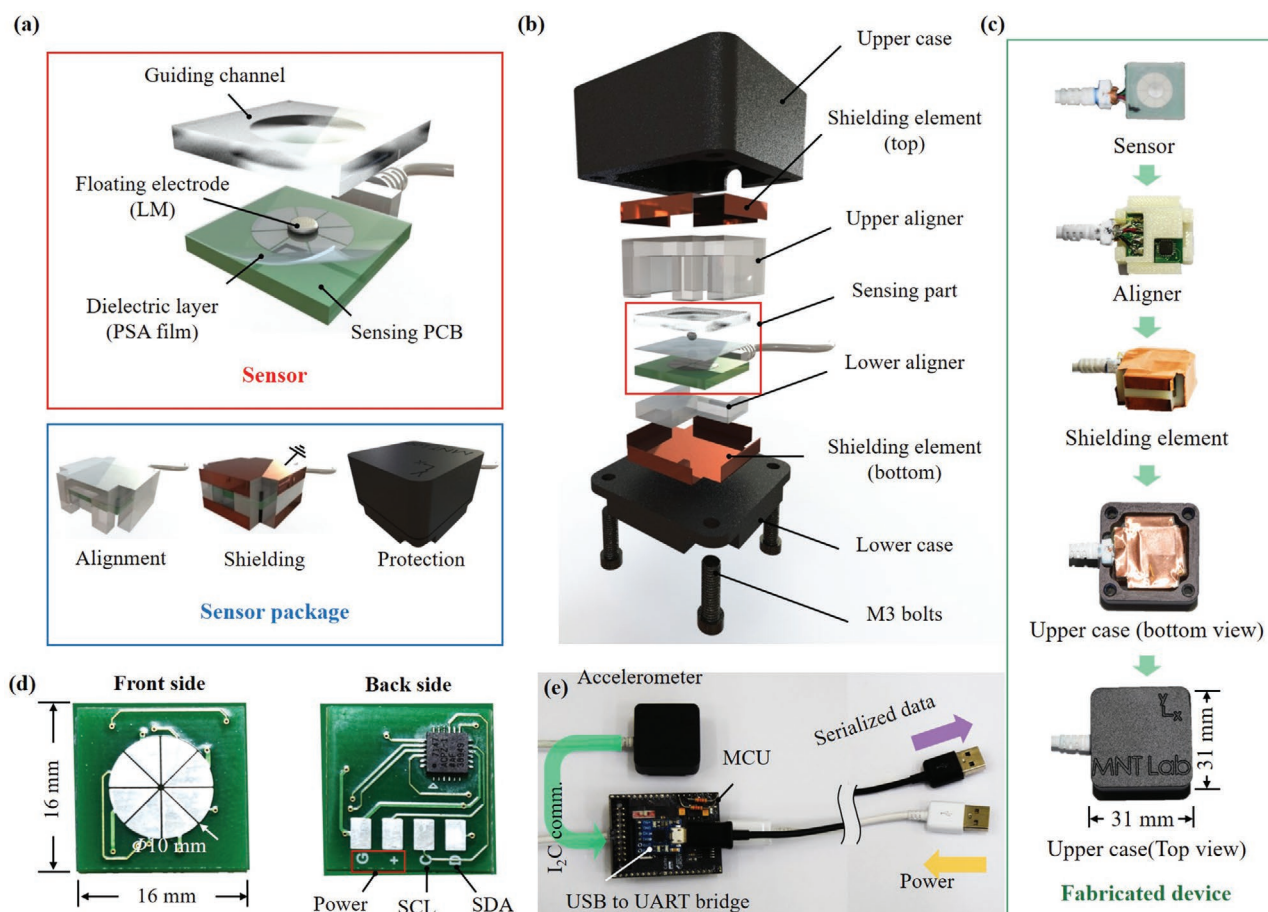


**Figure 2.** Overview of two-axis accelerometer: a) details of sensor and sensor package. b) An exploded diagram of our accelerometer. c) Process of sensor packaging and assembly. Modules of capacitive-type accelerometer: d) fabricated sensing PCB and e) entire measurement system including MCU and USB to UART bridge.

fixed by fastening the upper and lower cases via bolts. This fabrication process was performed in a relatively clean environment under atmospheric pressure (1 atm). An exploded view and the fabricated device are depicted in Figures 2b and 2c, respectively.

Owing to the development of a small capacitance-to-digital (C/D) converter chip, the measurement system of the capacitance has been recently miniaturized, and many capacitive-type devices are applied.<sup>[35–38]</sup> A measurement system using a C/D converter chip (AD7147) is also constructed. Here, the AD7147 chip can measure a total range of 20 pF with a resolution of 10 fF. The sensing rate is  $\approx 325$  Hz per cell when measuring four cells. When capacitance changes from  $\approx 4$  to 25 pF, the output of the counter varies linearly from  $\approx 0$  to 60 000. The PCB manufactured for sensing is shown in Figure 2d. The PCB size is  $16 \times 16$  mm<sup>2</sup>, and the electrodes are arranged on the front side. The AD7147 and electrodes for power supply and communication are arranged on the back side.

The configuration of the entire measurement system is shown in Figure 2e. The data from the AD7147 chip are sent to the MCU (Cortex-M3, ARM) using I<sub>2</sub>C communication which then sends serialized data to the PC using serial communication (USB port). Here, power (5 V) to the MCU is also supplied through another USB port.

### 3. Design of Spring Constant

The spring constant of the accelerometer is an important parameter affecting the performance (e.g., sensitivity and response characteristic) of the device. To achieve accurate performance of the device, it is necessary to set the spring constant by calculating the Laplace pressure at the position of the LM droplet.

As described in Section 3.1, a 2D mathematical model is used to calculate the Laplace pressure according to the position of LM droplet in various channel shapes. The location of the LM droplets with a known acceleration in the channel is recorded using a tilting stage. Additionally, the process of calculating the inertial force based on the tilting angle ( $\theta$ ) is described in Section 3.1.

The characteristic area, which is a parameter for directly comparing Laplace pressure and inertial force, is determined. By multiplying the Laplace pressure with characteristic area and converting it into a force unit, the magnitude can directly be compared to the inertial force. The procedure for calculating the characteristic area is described in Section 3.2.

To apply a certain acceleration, a custom-built tilting motorized rotary stage was constructed, as shown in Figure 3a. To

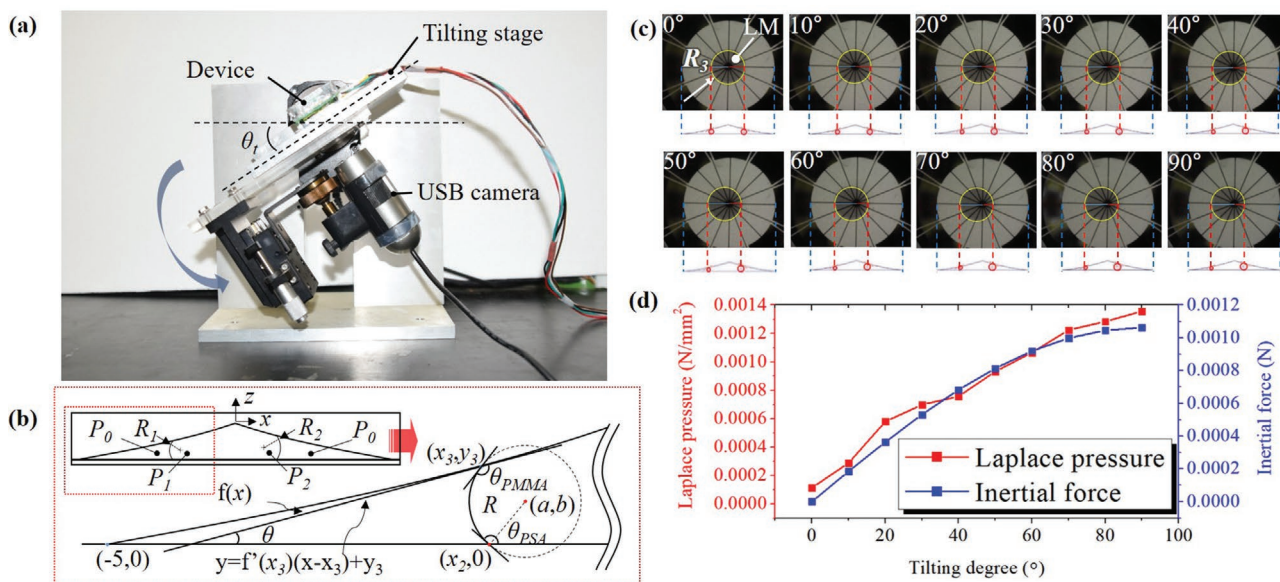


**Figure 3.** The setup for measuring the movement of a liquid metal droplet: a) custom-built tilting stage. Mathematical modeling used to predict the Laplace pressure induced in the guiding channel: b) a 2D mathematical model, c) captured image of liquid metal droplet between guiding channel and dielectric layer according to the acceleration, and d) comparison of Laplace pressure and inertia force according to the tilting angle of the stage.

observe the behavior of the LM droplet inside the guiding channel, a transparent test device was created, and a digital camera (AD7013MZT, Dino-Lite) was installed at the bottom. The bottom part of the device, including the sensing electrodes and dielectric layer, was fabricated via a common photo-lithography process on a glass substrate. The parts for fixing the device are composed of a transparent acrylic material. The tilting stage is accurately controlled using Labview software.

### 3.1. Laplace Pressure

Various mathematical models for predicting the behavior of a liquid droplet in 2D or 3D wedge plates under an applied acceleration have been proposed, and studies in this area have been actively conducted.<sup>[39,40]</sup>

Similarly, a simple 2D model was established to predict the Laplace pressure depending on the position of the LM droplet, as shown in Figure 3b. Based on the acceleration, its position was determined through tilting experiments and image processing (Figure 3c).

An observation of the LM droplet captured from the bottom shows that it maintains a nearly circular shape, owing to its high surface tension. Therefore,  $R_3$  is assumed to be constant. Therefore, in the Laplace pressure Equations (2) and (3) that are applied to both ends of the LM droplet,  $R_3$  can be eliminated. Thus, Equation (4) can be established.

$$P_0 - P_1 = \gamma(1/R_1 - 1/R_3) \quad (2)$$

$$P_0 - P_2 = \gamma(1/R_2 - 1/R_3) \quad (3)$$

$$P_2 - P_1 = \gamma(1/R_1 - 1/R_2) \quad (4)$$

where  $R_1$  and  $R_2$  are the vertical curvature radii of the left and right side of LM, respectively;  $R_3$  is the horizontal curvature radius of LM;  $P_0$  is pressure around the LM;  $P_1$  and  $P_2$  are the pressures at the left and right side interfaces of the LM, respectively;  $\gamma$  is the surface tension of the LM.

For (4),  $R_1$  and  $R_2$  must be known to calculate the Laplace pressure across the LM droplet. To obtain  $R_1$  and  $R_2$ , the contact position between the LM droplet and the bottom layer (i.e.,  $x_2$ ) according to  $\theta_t$  (Figure 3a) should be known, as shown in Figure 3b. This position can be obtained through image processing in the setup mentioned above. Assuming that the contact angle is maintained at the wall (i.e., the contact angle between the PSA film and LM droplet,  $\theta_{PSA}$ , and the contact angle between the adhesive PMMA guiding channel and the LM droplet,  $\theta_{PMMA}$ ),  $R_1$  can be obtained through  $x_2$ . The value of  $R_2$  can be obtained using the same method.

The inertia force applied to the LM droplet by  $\theta_t$  can be calculated by multiplying the mass of the LM droplet with acceleration applied in the axial direction, as shown in Equation (5).

$$F_{inertia} = \rho Vg \quad (5)$$

where  $\rho$ ,  $V$ , and  $g$  represent the density, volume, and acceleration due to gravity ( $9.81 \text{ m s}^{-2}$ ) of the LM droplet, respectively.

### 3.2. Characteristic Area

The volume of the device droplet ( $V$ ) is arbitrarily determined as  $8 \mu\text{L}$ . Through a tilting test, the characteristic area of the droplet ( $8 \mu\text{L}$ ) is determined by comparing the inertia force of the proof mass with Laplace pressure according to  $\theta_t$ . Here, the mass of LM droplet is clear, and thus the inertia force is accurate. The Laplace pressure is also reliable because it is based on  $x_2$

obtained through actual experiments. Therefore, the characteristic area is determined by dividing the inertia force by Laplace pressure. Assuming that the characteristic area of LM droplet is  $\approx 1 \text{ mm}^2$ , the graph of Laplace pressure and inertia force is similar (Figure 3d). Therefore, the characteristic area at  $8 \mu\text{L}$  is determined to be  $1 \text{ mm}^2$  (i.e., characteristic length of  $1 \text{ mm}$ ).

The Laplace pressure and inertia force according to  $\theta_t$  are compared in Figure 3d.

### 3.3. Droplet Volume

Here,  $V$  can be used to control the sensitivity because it determines the mass of LM droplet in the device. However,  $V$  also changes the ratio of kinetic energy to surface energy. This phenomenon causes the droplet to breakup when the accelerometer is driven at a high speed.<sup>[41]</sup> This erratic behavior of the droplet causes errors in the output values, making the design more difficult. Therefore,  $V$  is fixed to  $8 \mu\text{L}$ , and the feasibility is confirmed using the Weber number ( $We$ ), as shown in Equation (6):

$$We = \rho L U^2 / \sigma \quad (6)$$

where  $\rho$ ,  $L$ ,  $U$ , and  $\sigma$  represent the density, characteristic length, velocity, and surface tension of the LM droplet, respectively.

Additionally,  $We$  represents the ratio of the kinetic energy to the surface energy. When  $We < 3$ , the droplet maintains its shape without breakup.<sup>[41]</sup> For the volume of the proof mass ( $8 \mu\text{L}$ ) used in this study, as  $We$  is  $\approx 2.4$  when  $U$  is less than  $0.3 \text{ m s}^{-1}$ , it can be concluded to be a reasonable volume ( $\rho = 13.53 \text{ g cm}^{-3}$ ,  $L = 1 \text{ mm}$ , and  $\sigma = 0.487 \text{ N m}^{-1}$ ).

### 3.4. Channel Shape

The channel shape is defined as a function used to construct the inside of the channel from a convex to a concave form. The curvature of the channel wall is controlled with the diameter and height fixed at  $10$  and  $1 \text{ mm}$ , respectively. The gradient is controlled using Equation (7):

$$f(x) = \begin{cases} ((5-x)/5)^q, & \text{at } 0 \leq x \leq 5 \\ ((5+x)/5)^q, & \text{at } -5 \leq x < 0 \end{cases} \quad (7)$$

where  $f(x)$  is the function of the channel wall and  $q$  is the shape control variable which determines convex or concave shapes. The channels that have different gradients by changing  $q$  by  $1/2.5$ ,  $1/2$ ,  $1/1.5$ ,  $1$ ,  $1.5$ ,  $2$ , or  $2.5$  is fabricated. The shape of the guiding channel is convex when  $q$  is smaller than  $1$ , a straight line when  $q$  is  $1$ , and concave when  $q$  is larger than  $1$ . When  $q$  decreases, the channel shape becomes more convex, and conversely, the channel shape becomes more concave (Figure 4a) with an increase in  $q$ .

Each channel is applied to a mathematical model (Figure 3b) to analyze the change in Laplace pressure according to the channel, wherein, the displacement of the center ( $D_{\text{center}}$ ) of the LM droplet is defined in Figure 4b. As shown in Figure 5a,

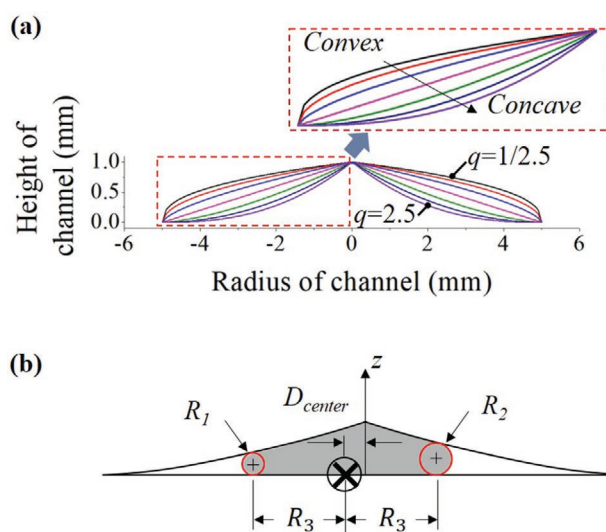


**Figure 4.** a) Various shapes of guiding channel according to the shape control variable  $q$  (refer to (7)) and b) definition of the center displacement ( $D_{\text{center}}$ ).

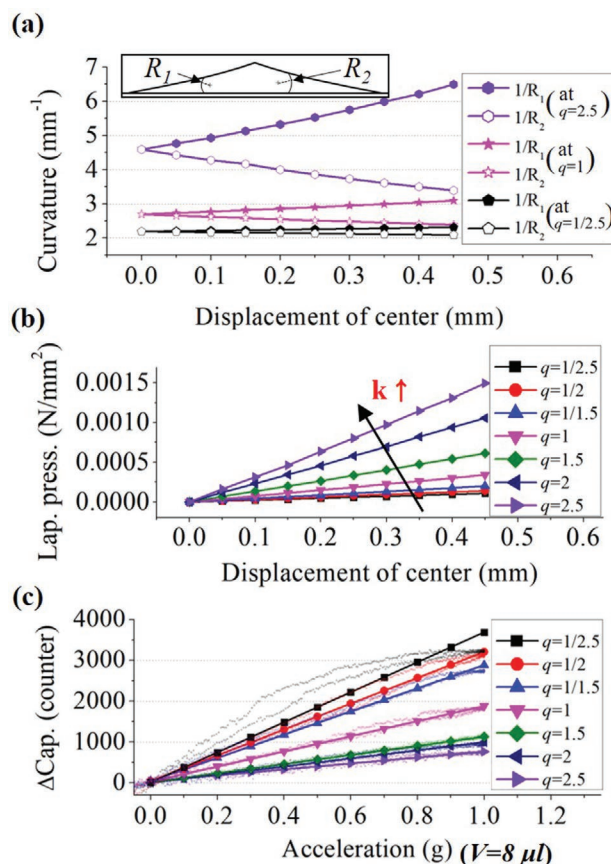


**Figure 5.** Effects of the channel shape on the sensitivity: a) estimation of the difference in curvature at both ends of the liquid metal droplet, b) Laplace pressure according to  $q$  from the mathematical model, and c)  $\Delta C$  change within the acceleration range of  $0$  to  $1 \text{ g}$  with change in shape of the guiding channel.

**Table 2.** The spring constants ( $k$ ) and non-linearity according to  $q$ .

$q$ [ $V = 8 \mu\text{L}$ ]	1/2.5	1/2	1/1.5	1	1.5	2	2.5
$k$ [ $\text{N m}^{-1}$ ]	0.28	0.36	0.52	0.92	1.76	2.94	4.71
Non-linearity [%]	26.8	9.4	7	7.7	5.9	14.1	13.6

as the channel shape becomes concave ( $q \uparrow$ ), the difference in curvature at both ends of the LM droplet is larger owing to the movement. This means that Laplace pressure increases (Figure 5b). By multiplying the Laplace pressure with characterization area ( $\approx 1 \text{ mm}^2$ ) and converting it into a force unit, the restoring force to the center according to the travel distance of LM (spring constant,  $k$ ) can be obtained.

To confirm changes in the device output, the  $\Delta C$  is measured within an acceleration range of 0 to 1 g by changing the shape of the guiding channel (Figure 5c). Raw data (semi-transparent dots) and linear fitted lines (to calculate non-linearity of raw data) are marked together. As shown from experimental results, when restoring force is stronger, sensitivity is decreased. Because the measurement range of acceleration and sensitivity are inversely proportional, adjusting the sensitivity to the desired acceleration measurement range is important. The spring constant ( $k$ ) and non-linearity according to  $q$  are summarized in Table 2. The sensitivity is tuned by simply replacing the guiding channel for the desired application. In case of convex channels, the hysteresis and non-linearity of the graph are increased when channel size is too large in comparison to the volume of the droplets, and hence is not good at guiding the droplets. In contrast, the curvature difference of both ends of the droplet increases non-linearly depending on the movement of the LM droplet in concave channels. The lowest non-linearity is 5.9% when  $q$  is 1.5 in a volume of  $8 \mu\text{L}$ .

## 4. Characterization

In this section, a few key characteristics of the device are analyzed. First, the cross-axis sensitivity of the device is confirmed to analyze the interference of each axis. Because the device measures two-axis accelerations using a single proof mass, it can be measured perpendicular to the acceleration direction regardless of the sensing axis. Second, the response time of the device is analyzed. All surfaces in contact with the liquid-type proof mass (i.e., the guiding channel and dielectric layer) are modified to shorten the response time. To confirm the effect of surface modification, the difference in the response time of the device and that of the commercial accelerometer is analyzed. Third, the shake-recoverable characteristic is confirmed. In conventional accelerometers that employ a solid-type proof mass, a large impact beyond the operating range results in permanent and irreversible damage. However, due to the inherent properties of the liquid, the accelerometer can be used again via a simple shaking motion, even if the LM droplet (i.e., proof mass) is fragmented due to the large impact. The shake-recoverable characteristic is confirmed experimentally. Finally, the reliability of the device is verified through a repeatability test for its application. After the verification, the device is applied to a maze escape game application to ensure that it is capable of

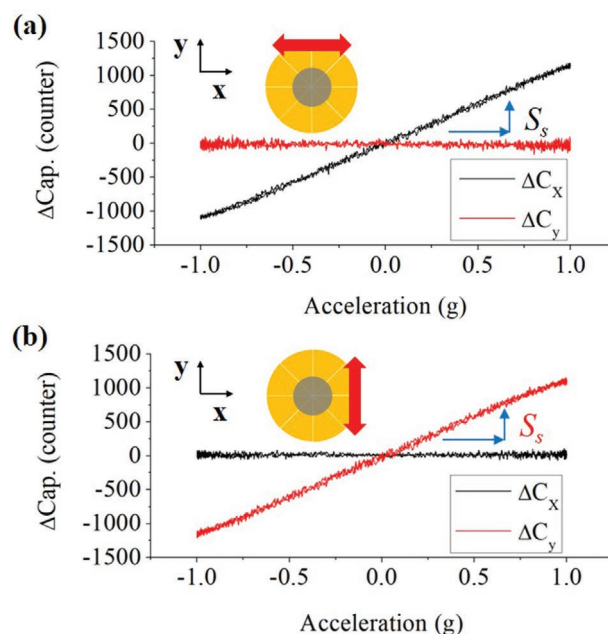


**Figure 6.** Sensitivity of the device along a)  $x$ - and b)  $y$ -axes.

measuring the two-axis acceleration in a stable manner. Here, the characterization is performed using the highest linearity device (i.e.,  $q = 1.5$ ).

### 4.1. Cross-Axis Sensitivity

A tilting test is conducted to confirm the cross-axis sensitivity of the device, which is defined as the sensitivity of the plane perpendicular to the measurement direction relative to the sensitivity in the measurement direction itself and is expressed as Equation (8).

$$S_c = (S_p/S_s) \times 100 \quad (8)$$

where  $S_c$  is the cross-axis sensitivity,  $S_p$  is the sensitivity of the axis perpendicular to the sensing axis (i.e., the off-sensing axis), and  $S_s$  is the sensitivity of the principal sensing axis.

To obtain  $S_c$ , the values of  $S_p$  and  $S_s$  for each axis should first be obtained. When the range of acceleration changes from  $-1$  to  $1$  g along the  $x$ -axis,  $\Delta C_x$  changes from  $\approx -1020$  to  $1050$  counters, whereas  $\Delta C_y$  barely changes (Figure 6a). Because the LM droplet moves along the  $x$ -axis, the difference in the overlapped area between the opposing  $x$ -axis cell pairs increases; thus,  $\Delta C_x$  changes significantly. Moreover, because of the changes in the overlapped area of the opposing  $y$ -axis, the cell pairs are almost identical; the difference in the overlapped area reaches almost zero, and  $\Delta C_y$  only exhibits a minor change. Similarly, for the acceleration along the  $x$ -axis, when the range of acceleration changes from  $-1$  to  $1$  g along the  $y$ -axis,  $\Delta C_y$  changes significantly; however,  $\Delta C_x$  only changes marginally (Figure 6b). To obtain  $S_s$  and  $S_p$  for each axis, linear fitting is applied to obtain the slope of the fitted line. The values of  $S_s$ ,  $S_p$ , and  $S_c$  for each axis are summarized in Table 3. Both axes have a cross-axis sensitivity of less than 1%. The results indicate that two-axis

**Table 3.** Performance of developed accelerometer.

Test parameter [units]	x-axis	y-axis
$S_x$ [counter $g^{-1}$ ]	$\approx 1044$	$\approx 1059$
$S_y$ [counter $g^{-1}$ ]	$\approx 2$	$\approx 8$
Cross-axis sensitivity [%]	$\approx 0.2$	–
	–	$\approx 0.8$

acceleration can be measured with little interference for the  $x$ - and  $y$ -axes.

#### 4.2. Surface Modification and Response Time

To increase mobility of the LM droplet, the surfaces of guiding channel (PMMA) and dielectric layer (PSA) were modified using a sandblasting method due to which they are uniformly covered with microstructures (Figure 7a), whereas the unmodified surfaces are smooth (Figure 7b). To confirm the effects of surface modification on droplet behavior, the static and dynamic wettability of the LM droplet ( $\approx 4 \mu\text{L}$ ) is analyzed. The contact angle hysteresis (CAH), which differs between advancing and receding angles, is measured using the tilting method, and sliding angle (SA), which is the tilted stage angle when the droplet starts to move, is also measured using a contact angle meter (SmartDrop, Femtobiomed, Inc.). The measured wettability results are summarized in Table 4. CAH and SA are significantly reduced on the modified surfaces instead of bare surfaces. Thus, using a modified surface can make the LM droplet move easily in the channel.

To analyze the effects of increased mobility of the droplet through surface modification, the response time of the device is compared with a commercial accelerometer (ADXL345, Analog

Device) based on a random acceleration test. These accelerometers are mounted on a sliding test setup and randomly accelerated (Figure 7c). The output data of both accelerometers are simultaneously saved using Labview software. This experiment was conducted for 30 s, and the two accelerometers were compared in terms of the acceleration. The datasets of both accelerators were similar (Figure 7d, Movie S2, Supporting Information).

The data between 5 and 7 s is analyzed to determine the difference between the two accelerometers (the green box in Figure 7d, which confirms that the response time delay between the accelerometers and the commercial accelerometers is less than 30 ms. A simple shock test was conducted to confirm the performance at the high acceleration ( $\approx 16 \text{ g}$ ) (Figure S1, Supporting Information). The result demonstrates that the accelerometer has a measurable limit of  $\approx 5 \text{ g}$  (Figure S2, Supporting Information).

#### 4.3. Allan Variance

Bias variations are caused by various random processes during device operation.<sup>[42]</sup> Allan variance is used for analyzing device errors. Biases are measured by averaging a finite sequence of samples when a device is in idle position. Explanatively, a long sequence (24 h) of data is taken, and then divided into bins based on an average time. The function for Allan variance is as shown in Equation (9).

$$\text{AVAR}^2(\tau) = \frac{1}{2(n-1)} \sum_i (\gamma(\tau)_{i+1} - \gamma(\tau)_i)^2 \quad (9)$$

where AVAR ( $\tau$ ) is the Allan variance written as a function of the average time,  $\tau$ ,  $\gamma_i$  is the average value of measurement

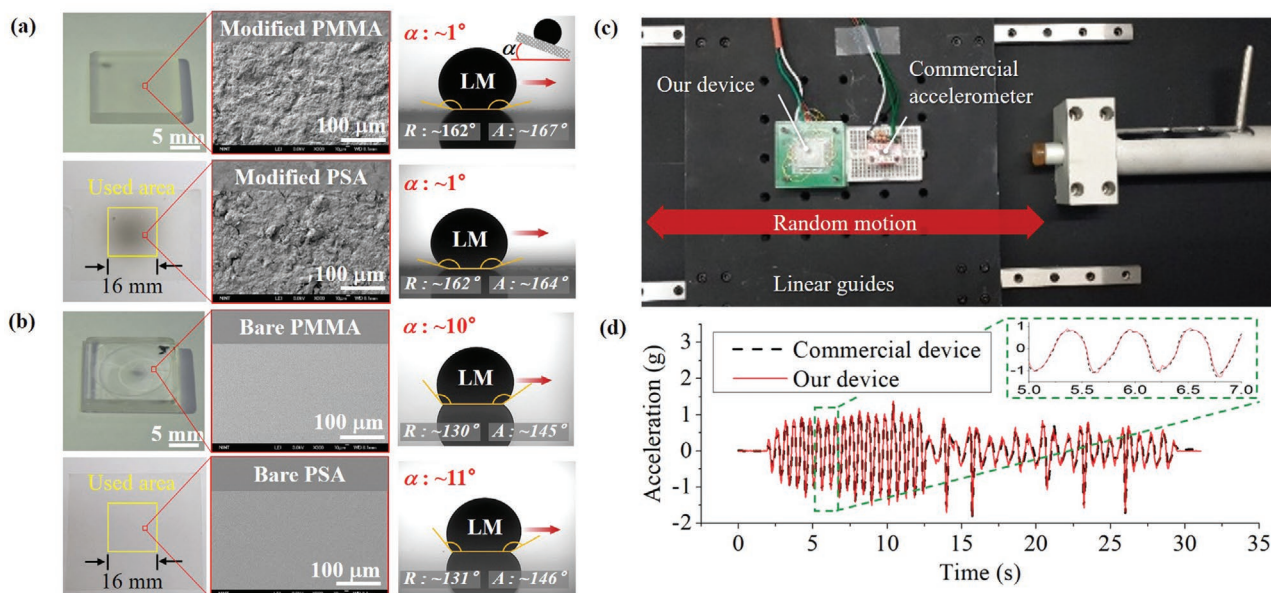


**Figure 7.** Effects of surface modification: a) a modified and b) un-modified surfaces of PMMA guiding channel and adhesive PSA film. Effects of increased mobility of the droplet through the surface modification: c) sliding test setup and d) comparison data between our device and a commercial device with randomly applied motions.

**Table 4.** Wettability of LM droplet on the modified and unmodified surfaces of PMMA and PSA.

	Contact angle [°]			CAH [°]	SA [°]
	Static	Advancing	Receding		
Modified PMMA	≈165	≈167	≈162	≈5	≈1
Modified PSA	≈163	≈164	≈162	≈2	≈1
Bare PMMA	≈136	≈145	≈130	≈15	≈10
Bare PSA	≈137	≈146	≈131	≈15	≈11

in bins  $i$ , and  $n$  is the total number of bins. **Figure 8a** shows Allan variance curve of the device. The bias instability, which is defined as the best stability with a fully modeled sensor and active bias estimation, is the minimum point on the Allan variance curve. The device is within 0.185 mg of bias instability with ≈70 s averaging time. The bias over the entire time (1 sigma) can be called as in-run instability, and this value of the device is ≈3.325 mg. At short average intervals, the Allan variance is dominated by the noise in the device. There is a direct correlation between standard deviation (the noise) of the output versus time and the slope of Allan variance for smaller values of  $\tau$ . This is also referred as velocity random walk (VRW). The developed device shows 3.272 mg/rt-Hz of VRW. Bias instability, in-run instability, and VRW of the developed device are summarized in **Table 5**.

#### 4.4. Temperature Behavior

To analyze the temperature behavior of the device, it is mounted in a temperature chamber and the output is analyzed. **Figure 8b** shows the relationship of the output converted into gravity versus temperature of the device. Here, the temperature varies from -20 to 60 °C (1 cycle, 520 m). In this paper,

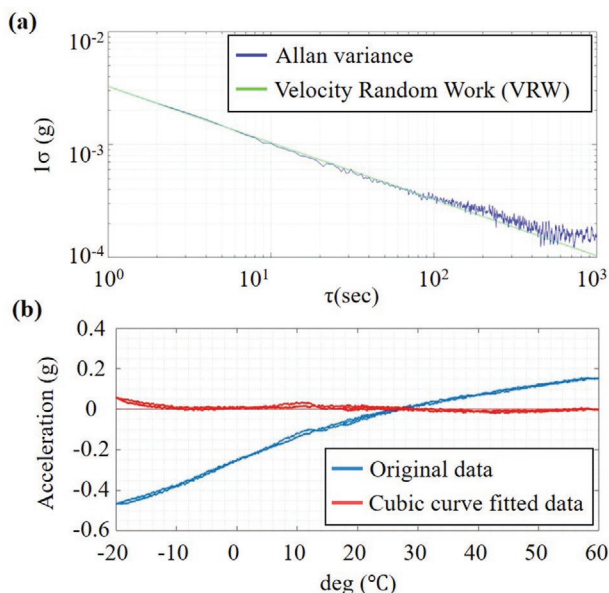


**Figure 8.** a) Allan variance analysis. b) Relationship of the output converted into gravity versus temperature of the device.

**Table 5.** Bias instability, in-run instability, velocity random walk, and temperature behavior of developed accelerometer.

Bias instability	0.185 mg
In-run instability	3.325 mg
VRW	3.272 mg/rt-Hz
Temperature sensitivity	8.2 mg deg <sup>-1</sup>
Temperature hysteresis	20 mg

temperature sensitivity is defined as the change in output of the device with changing temperature conditions. Temperature sensitivity can be obtained from the slope of original data (blue line); the device shows ≈8.2 mg deg<sup>-1</sup> of temperature sensitivity. The original data (blue line) was fitted with a cubic curve (red line) to indicate the change in hysteresis of the device output with temperature. Through the fitted graph ≈20 mg of temperature hysteresis of the device is confirmed. Temperature sensitivity and hysteresis of the developed device are summarized in **Table 5**. For a more detailed analysis, experiments on sensitivity change based on temperature are discussed in **Figure S3**, Supporting Information.

#### 4.5. Shake-Recoverable Characteristic

To confirm the shake-recoverable characteristic, the accelerometer is mounted on the sliding test setup as mentioned above and subjected to a shock to separate the LM droplets. The images of the LM droplet before and after the shock, and pursuant to shaking are shown in **Figure 9a**. After the shock, the LM droplet is separated into large and small droplets. However, after the shaking, the separated LM droplets merge into a single droplet. With this healed accelerometer, a tilting test is conducted to confirm that it works again. The output of the healed accelerometer after shaking matches with that of the accelerometer before the shock.

Recognizing the destruction of LM proof mass is a considerably important issue because the device's performance changes when the LM is destroyed. If this is not recognized, the device outputs an abnormal acceleration value. A typical recognition method is to consider the fact that volume of the proof mass is reduced when the LM is destroyed. When LM reduces, the total sum of capacitances measured in each cell ( $C_{total} = C_{xR} + C_{xL} + C_{yU} + C_{yD}$ ) is reduced. The relevant data has been added to **Figure 9b**, which shows that the device with high impact (free-fall from 1 m height), the  $C_{total}$  is reduced by more than 50 Counter, when the LM is finely destroyed. More details about the shock test are provided in Supporting Information S1. However, after shaking the LM three times with an acceleration of 1 g (shaking within the range that the counter of  $\Delta C_x (= C_{xR} - C_{xL})$  and  $\Delta C_y (= C_{yU} - C_{yD})$  does not exceed 1000 (counter at ≈1 g)), it heals again and  $C_{total}$  returns to its original value.

## 5. Application

Before applying the device to its application, the repeatability should be checked to verify its reliability. To confirm the

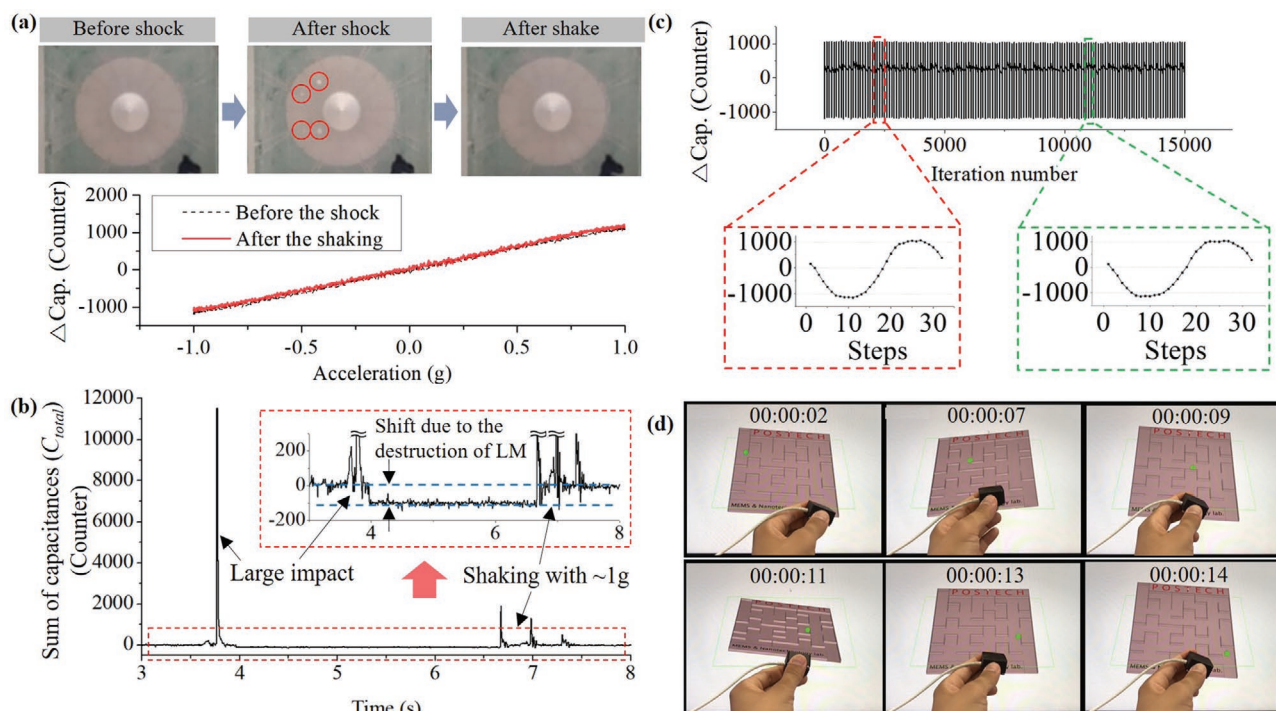


**Figure 9.** Shake-recoverable test. a) Images of the LM droplet before the shock, after the shock, and after the shaking. The output of the accelerometer before shock, and the recovered accelerometer after shaking. b) Sum of capacitances shift due to the destruction of the LM droplet. Results of c) repeatability test and d) maze escape game application.

repeatability of the accelerometer, a cycle test is conducted using the tilting test setup. For reliability, the results showed a change in peak value of output less than 1.4% of the 15000th cycle (Figure 9c).

Based on this reliability, the developed two-axis accelerometer is applied to a 3D maze escape game. The game environment was programmed using PROCESSING software. The plate is tilted in proportion to the amount of  $x$ - and  $y$ -acceleration, and the ball in the maze moves according to the direction and degree of tilt. The maze plate is tilted in various directions according to the tilting direction of acceleration and the game was successfully played (Figure 9d, Movie S3, Supporting Information).

## 6. Discussion and Conclusion

In this paper, a two-axis measurable capacitive-type accelerometer using a liquid metal droplet as a proof mass is proposed. The capacitance is measured using a floating electrode concept. This structure has a significant advantage in terms of increasing the mobility of liquid metal droplets. Because the dielectric layer completely covers the electrodes, it can modify the contact surface of the liquid metal droplet without damaging the electrodes. The position of the liquid metal droplet is estimated by sensing a change in overlapped area between the electrodes and itself. To control the sensitivity of the device, using a liquid-type proof mass, the correlation between Laplace pressure generated by the channel and liquid metal droplet was identified through 2D mathematical modeling. The effects of channel shape on

sensitivity is also analyzed using a mathematical model. Linearity is different for each channel and with a specific channel the linearity is over 94% in the range between  $-1$  to  $1$  g. To confirm the effect of sandblasting, the response time of the device was compared with a commercial accelerometer. Moreover, the signal output of the device, with and without sandblasting under the same acceleration was compared, and it was noted that signal of the device without sandblasting has a time delay of  $\approx 25$  ms as compared with sandblasting. Additionally, it was also confirmed that the device with sandblasting has a higher sensitivity than that without. Therefore, the reason for comparable sensitivity and response time to that of the commercial accelerometers is due to increased mobility of the LM droplet from sandblasting applied to the dielectric layer. The various characteristics of the fabricated device were analyzed (i.e., the cross-axis sensitivity, response time, shake-recoverable characteristic, temperature behavior and repeatability). It was observed, that not only does the proof mass heal, but its detection of being destroyed is very important, and if left unrecognized, can affect device performance. It was noted that, when destroyed, the LM loses its total volume. Experimentally, when a large impact was applied, the output in the whole cell decreased, but the signal recovered again after shaking with an acceleration of about  $1$  g. The volume of LM also affected the ratio of inertial force to surface tension, which was important in determining the strength of impact for LM to be destroyed. It also affected the device's sensitivity change. Further study on other impacts of LM volume, will be done in our future work. Finally, the device is applied to a maze escape game application and confirmed that it can stably measure the two-axis acceleration.

The device may be useful in harsh environments where it is frequently exposed to unexpected shocks (over the sensor's measurement range) or where fatigue is easily experienced. However, it is difficult to repair or periodically replace the device.

Received: November 14, 2019

Revised: March 6, 2020

Published online:

## 7. Experimental Section

**Preparation of Liquid Metal Droplets:** To produce LM droplets of a certain volume, a glass plate with a groove of the desired volume was prepared using a milling machine. Thereafter, the LM with a volume greater than the target volume was placed on the grooved glass plate, and squeezed using a flat glass. Thus, after removing the flat glass, the LM with desired volume remained in the groove; this volume of LM was subsequently taken out to the guiding channel.

**Fabrication of Dielectric Layer:** A single-sided pressure sensitive adhesive (PSA) tape (#9964, 3M) with a thickness of  $\approx 60 \mu\text{m}$  and a relative dielectric constant of  $\approx 3.2$  was used as the dielectric layer.

**Fabrication of Guiding Channel:** The guiding channel was fabricated using a poly methyl methacrylate (PMMA) hot-embossing method with an aluminum mold. The mold consisted of parts that determine the internal shape of the channel, and an aluminum plate with holes corresponding to these parts. After fabricating the concave- and convex-shaped parts by using the lathe, the molds were made by assembling the parts to the aluminum plate with holes.

**Fabrication of Aligner:** The aligners (ABS material) were fabricated using a 3D printer (uprint SE plus, Stratasys).

**Fabrication of Protection Cases:** The protection cases were fabricated with aluminum using a 3D milling machine.

**Fabrication of Transparent Bottom Layer:** The bottom part of the device, including the sensing electrodes and dielectric layer, was fabricated using a common photo-lithography process on a glass substrate. Thereafter, a surface modified PSA film was attached to it.

**The Operating Condition of Sandblasting:** The operating conditions of the sandblaster varied according to the surface hardness of the material: The PMMA was at 0.3 MPa for 10 s, and the PSA at 0.1 MPa for 3 s. The distance between the specimen and nozzle of the sandblaster was maintained at  $\approx 7 \text{ cm}$ .

## Supporting Information

Supporting Information is available from the Wiley Online Library or from the author.

## Acknowledgements

This research was supported by a grant of the Korea Health Technology R&D Project through the Korea Health Industry Development Institute (KHIDI), funded by the Ministry of Health and Welfare, Republic of Korea (Grant No. HI15C0001).

## Conflict of Interest

The authors declare no conflict of interest.

## Keywords

capacitive-type sensors, Laplace pressure, liquid metals, healing materials, surface modification

- [1] G. Krishnan, C. U. Kshirsagar, G. K. Ananthasuresh, N. Bhat, *J. Indian Inst. Sci.* **2007**, *87*, 333.
- [2] D. K. Shaeffer, *IEEE Commun. Mag.* **2013**, *51*, 100.
- [3] Q. Li, D. Xiao, Z. Hou, X. Wang, Z. Chen, X. Wu, *2015 IEEE SENSORS, IEEE*, Busan, South Korea **2015**.
- [4] X. Zhou, L. Che, S. Liang, Y. Lin, X. Li, Y. Wang, *Microelectron. Eng.* **2015**, *131*, 51.
- [5] C. M. Sun, C. Wang, W. Fang, *Sens. Actuators, A* **2008**, *141*, 347.
- [6] T. Gomathi, S. M. Shaby, 2016 International conference on control, instrumentation, communication and computational technologies (ICCICCT), *IEEE*, Kumaracoil, India **2016**, 486.
- [7] Z. Mohammed, I. M. Elfadel, M. Rasras, *Micromachines* **2018**, *9*, 602.
- [8] I. Zeimpekis, I. Sari, M. Kraft, *J. Microelectromech. Syst.* **2012**, *21*, 1032.
- [9] O. Aydin, T. Akin, *IEEE Sens. J.* **2012**, *13*, 2914.
- [10] D. Yamane, T. Matsushima, T. Konishi, H. Toshiyoshi, K. Masu, K. Machida, *Microsyst. Technol.* **2016**, *22*, 459.
- [11] M. Zakriya, D. Ghada, C. Aveek, R. Mahmoud, *Mechatronics* **2018**, *54*, 203.
- [12] C. M. Sun, M. H. Tsai, Y. C. Liu, W. Fang, *IEEE Trans. Electron Devices* **2010**, *57*, 1670.
- [13] M. H. Tsai, Y. C. Liu, W. Fang, *J. Microelectromech. Syst.* **2012**, *21*, 1329.
- [14] M. A. Lemkin, B. E. Boser, D. Auslander, J. H. Smith, *In Proceedings of the International Conference on Solid State Sensors and Actuators Conference*, Chicago, IL, USA **1997**.
- [15] A. Partridge, J. K. Reynolds, B. W. Chui, A. M. Fitzgerald, L. Zhang, N. I. Maluf, T. W. Kenny, *J. Microelectromech. Syst.* **2000**, *9*, 58.
- [16] H. S. Hsieh, H. C. Chang, C. F. Hu, C. L. Cheng, W. Fang, *J. Micro-mech. Microeng.* **2011**, *21*, 105006.
- [17] U. Park, J. Rhim, J. U. Jeon, J. Kim, *Microelectron. Eng.* **2014**, *129*, 5.
- [18] J. Zhang, Y. Su, Q. Shi, A. P. Qiu, *Sensors* **2015**, *15*, 30293.
- [19] A. G. Krause, M. Winger, T. D. Blasius, Q. Lin, O. Painter, *Nat. Photonics* **2012**, *6*, 768.
- [20] F. Guzmán Cervantes, L. Kumanchik, J. Pratt, J. M. Taylor, *Appl. Phys. Lett.* **2014**, *104*, 221111.
- [21] G. Langfelder, S. Dellea, F. Zaraga, D. Cucchi, M. A. Urquía, *IEEE Trans. Ind. Electron.* **2012**, *59*, 4938.
- [22] S. Mariani, A. Ghisi, F. Fachin, F. Cacchione, A. Corigliano, S. Zerbini, *Meccanica* **2008**, *43*, 469.
- [23] D. H. Alsem, O. N. Pierron, E. A. Stach, C. L. Muhlstein, R. O. Ritchie, *Adv. Eng. Mater.* **2007**, *9*, 15.
- [24] G. Langfelder, S. Dellea, F. Zaraga, D. Cucchi, M. A. Urquía, *IEEE Trans. Ind. Electron.* **2012**, *59*, 4938.
- [25] X. Xiong, Y.-L. Wu, W.-B. Jone, *IEEE International Symposium on Defect and Fault Tolerance in VLSI Systems*, Arlington, VA, USA **2006**.
- [26] X. Xiong, Y.-L. Wu, W.-B. Jone, *IEEE International Symposium on Defect and Fault Tolerance of VLSI Systems*, Boston, MA, USA **2008**.
- [27] V. A. Hong, S. Yoneoka, M. W. Messana, A. B. Graham, J. C. Salvia, T. T. Branchflower, E. J. Ng, T. W. Kenny, *J. Microelectromech. Syst.* **2015**, *24*, 351.
- [28] U. Park, B. Park, I. Moon, D. Kim, J. Kim, *Microelectron. Eng.* **2011**, *88*, 276.
- [29] A. Garraud, A. Giani, P. Combette, B. Charlot, M. Richard, *Sens. Actuators, A* **2011**, *170*, 44.
- [30] B. Zhang, L. Zhang, W. Deng, L. Jin, F. Chun, H. Pan, B. Gu, H. Zhang, Z. Lv, W. Yang, Z. L. Wang, *ACS Nano* **2017**, *11*, 7440.

- [31] U. Park, K. Yoo, J. Kim, *Sens. Actuators, A* **2010**, 159, 51.
- [32] M. Huh, D. Won, J. G. Kim, J. Kim, *Micro Nano Syst. Lett.* **2017**, 5, 5.
- [33] K. Yoo, U. Park, J. Kim, *Sens. Actuators, A* **2011**, 166, 234.
- [34] D. Won, S. Baek, M. Huh, H. Kim, S. Lee, J. Kim, *Sens. Actuators, A* **2017**, 259, 105.
- [35] U. Kim, Y. B. Kim, D.-Y. Seok, J. So, H. R. Choi, *IEEE Trans. Ind. Electron.* **2017**, 65, 2755.
- [36] U. Kim, Y. B. Kim, J. So, D.-Y. Seok, H. R. Choi, *IEEE Trans. Ind. Electron.* **2018**, 65, 9604.
- [37] U. Kim, D. Lee, Y. B. Kim, D.-Y. Seok, J. So, H. R. Choi, *IEEE/ASME Trans. Mechatronics* **2017**, 22, 1717.
- [38] P. Hu, J. Guo, J. Tan, *IEEE Trans. Ind. Electron.* **2016**, 63, 2469.
- [39] C. Luo, X. Heng, M. Xiang, *Langmuir* **2014**, 30, 8373.
- [40] E. Ruis-Gutierrez, C. Semperebon, G. McHale, R. Ledesma-Aguilar, *J. Fluid Mech.* **2018**, 842, 26.
- [41] Y. Chen, E. P. DeMauro, J. L. Wagner, M. Arienti, D. R. Guildenbecher, P. A. Farias, T. W. Grasser, *55th AIAA Aerospace Sciences Meeting*, AIAA, Grapevine, United States **2017**.
- [42] A. Kos, S. Tomažič, A. Umek, *Sensors* **2016**, 16, 301.